Quantitative Contribution of Oxygen Vacancy Defects to Arsenate Immobilization on Hematite

Juan Liu, Yongjin Xiang, Yiwen Chen, Hongjun Zhang, Bangjiao Ye, Lu Ren, Wenfeng Tan, Andreas Kappler, and Jingtao Hou*

Read Online

ACCESS | Metrics & More | Article Recommendations | Supporting Information

ABSTRACT: Hematite is a common iron oxide in natural environments, which has been observed to influence the transport and fate of arsenate by its association with hematite. Although oxygen vacancies were demonstrated to exist in hematite, their contributions to the arsenate immobilization have not been quantified. In this study, hematite samples with tunable oxygen vacancy defect (OVD) concentrations were synthesized by treating defect-free hematite using different $NaBH_4$ solutions. The vacancy defects were characterized by positron annihilation lifetime spectroscopy, Doppler broadening of annihilation radiation, extended X-ray absorption fine structure (EXAFS), thermogravimetric mass spectrometry (TG-MS), electron paramagnetic resonance (EPR), and X-ray photoelectron spectroscopy (XPS).

The results revealed that oxygen vacancy was the primary defect type existing on the hematite surface. TG-MS combined with EPR analysis allowed quantification of OVD concentrations in hematite. Batch experiments revealed that OVDs had a positive effect on arsenate adsorption, which could be quantitatively described by a linear relationship between the OVD concentration (C_{def}, mmol m^{-2}) and the enhanced arsenate adsorption amount caused by defects (ΔQ_m, μmol m^{-2}) ($\Delta Q_m = 20.94\, C_{def}$, $R^2 = 0.9813$). NH_3-diffuse reflectance infrared Fourier transform (NH_3-DRIFT) analysis and density functional theory (DFT) calculations demonstrated that OVDs in hematite were beneficial to the improvement in adsorption strength of surface-active sites, thus considerably promoting the immobilization of arsenate.

KEYWORDS: hematite, oxygen vacancy, quantification, arsenate, immobilization
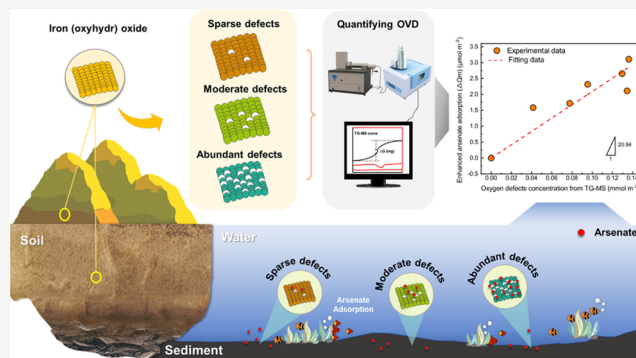
1. INTRODUCTION

Arsenic (As) is a metalloid commonly found in polluted soils and groundwaters that has high toxicity and carcinogenicity, which might increase incidences of cancer, along with other negative health effects. Moreover, the migration of arsenic in the environment further increases its environmental risks.[1−5] Abundant iron-bearing minerals in soils and sediments significantly affect the migration and fate of arsenic.[6,7] Hematite (α-Fe_2O_3) is one of the most common iron oxides that is widely distributed in tropical and subtropical regions. Due to its thermodynamic stability and high reactivity, hematite extensively participates in biogeochemical processes (e.g., via adsorption, oxidation/reduction, and catalytic processes) that have attracted much attention.[8−12] However, hematite hardly exists in perfectly crystalline form in natural environments due to the incorporation of impurities (e.g., Al and Mn ions) and the dynamic changes of environmental conditions (e.g., temperature), including redox conditions (e.g., via flooding and drainage),[13−15] which allows hematite to possess different vacancy defects, thereby showing varying physical and chemical properties.

In general, the reported literature divides the vacancy defects in minerals into two categories of anionic (e.g., $TiO_{2−x}$ and $ZrO_{2−x}$)[16,17] and cationic vacancies (e.g., $Cu_{2−x}O$ and $Fe_{1−x}O$).[18,19] It has been observed that the vacancy defects in iron oxides play an important role in the processes of oxidation/reduction, adsorption, electron transfer, and mineral microbial reduction.[20−22] For example, Notini et al. investigated experimentally the role of defects in Fe(II)−goethite electron transfer using a combination of techniques, such as ^{57}Fe Mössbauer spectroscopy, synchrotron-based X-ray absorption, and magnetic circular dichroism.[22] They found that low-temperature Fe(III) hydrolysis led to goethite particles possessing Fe vacancies, which could enable Fe-(II)−goethite electron transfer. These Fe vacancy defects were

also observed to considerably promote microbial goethite reduction, i.e., Fe vacancy-rich goethite exhibited large initial Fe(III) reduction rate relative to Fe vacancy-poor goethite.[21] Moreover, Liang et al. confirmed that Fe vacancy defects in hematite significantly increased lead and arsenic adsorption, which was explained by the large affinity constants and more adsorption sites induced by Fe vacancy defects.[14] To sum up, vacancy defects exhibit extremely important contributions to the interfacial reactivities of iron (oxyhydr)oxides. However, most of the reported literature only focus on the role of Fe vacancies, and very few studies have investigated whether the anionic vacancies (e.g., oxygen vacancies) also affect the mineral's physical and chemical properties. Moreover, current research mainly described the qualitative effect of vacancy defects on the physical and chemical properties, and their quantitative contributions are still unclear.

As Fe-bearing minerals have been reported as a sink of arsenic that controls the migration and fate of arsenic in natural environments,[23−25] uncovering the quantitative contribution of oxygen vacancy defects to arsenic immobilization by iron (oxyhydr)oxides is therefore of environmental significance to understand the fate of toxic arsenic in soils and sediments. Herein, hematite samples with different levels of oxygen vacancy defects were prepared by a facile reaction between defect-free hematite and $NaBH_4$ solutions at room temperature by adding different $NaBH_4$ concentrations. The defect characteristics of hematite samples were characterized by electron paramagnetic resonance (EPR), X-ray photoelectron spectroscopy (XPS), positron annihilation lifetime spectrometry (PAL), extended X-ray absorption fine structure (EXAFS), and Doppler broadening of annihilation radiation (DBAR). The objectives of this study are to (1) establish an approach to quantitatively measuring oxygen vacancy defect (OVD) concentrations in defective hematite, (2) evaluate the quantitative contributions of vacancy defects to arsenate immobilization, and (3) reveal the underlying mechanism of the effect of OVDs on arsenate adsorption.

2. MATERIALS AND METHODS

2.1. Mineral Preparation. Hematite was prepared by a precipitation approach following Schaller et al.[26] To obtain defect-free hematite (denoted as H-0M), the obtained sample was further calcined at 600 °C in an air atmosphere for 5 h to remove the impurities (e.g., amorphous iron oxide phases and defects). The defective hematite samples with tunable oxygen vacancy defect concentrations were prepared through the treatment of defect-free hematite samples using $NaBH_4$ solutions as reported by Sun et al.[27] Details of all sample preparation procedures are presented in Text S1.

2.2. Mineral Characterizations. The phase structure, morphology, mineral surface chemical valence, and defect characteristics of hematite samples were investigated by X-ray diffraction (XRD), scanning electronic microscopy (SEM), transmission electronic microscopy (TEM), N_2 adsorption/desorption curves, energy dispersion spectrum (EDS) mapping, electron paramagnetic resonance (EPR), X-ray photoelectron spectrometry (XPS), Doppler broadening of annihilation radiation (DBAR), positron annihilation lifetime spectrometry (PAL), synchrotron X-ray absorption spectroscopy (XAS), Raman spectra, in situ attenuated total reflectance-Fourier transform infrared (ATR-FTIR), and in situ diffuse reflectance infrared Fourier transform (DRIFT)

spectroscopy with NH_3 as a probe molecule. Detailed characterization procedures are described in Text S2.

2.3. Quantification of OVD Concentration on Hematite. In principle, when oxygen vacancy-containing hematite samples are placed in an oxygen atmosphere, the oxygen vacancies are readily refilled by gas-oxygen molecules at a relatively high temperature (e.g., 400−500 °C), thereby causing a certain increase of weight in defective hematite samples.[28] Thermogravimetric (TG) analysis is a useful tool to record the subtle weight change (accuracy of 0.00001 g) of minerals, while a mass spectrometer (MS) allows a precise tracking of the molecular signals during the subtle weight change of the sample. Therefore, thermogravimetric analysis combined with mass spectrometry (TG-MS) was employed to quantitively determine the OVD concentration in the defective hematite samples. Details of this approach are presented in Text S3.

2.4. Arsenate Adsorption Experiments. Arsenate batch adsorption experiments were performed on a thermostatic shaker with a velocity of 280 rpm at 25 °C. 0.01 M KNO_3 was used as a background electrolyte. Before the adsorption experiment, the hematite suspensions (0.3 g L^{-1}) were prepared and stirred on a magnetic mixer for 24 h. Then, As(V) solutions (10 mL) with concentrations varying from 0 to 0.67 mM and 10 mL hematite suspensions were mixed into a series of 50 mL polyethylene tubes. The mixtures were purged with high-purity dinitrogen to eliminate CO_2. The solution pH was adjusted to 6.0 using HCl (0.1 M) and NaOH (0.1 M). In the adsorption process, the solution pH was adjusted every 8 h to maintain pH stability. After 24 h, the mixtures were centrifuged at a speed of 12,000 rpm for 5 min, and the supernatant was filtered through a 0.22 μm filter membrane. The filtrates were collected to detect the residual As concentrations using an atomic fluorescence spectrometer (AFS-9700).[29]

2.5. Density Functional Theory (DFT) Calculations. The effect of vacancy defects on arsenate adsorption on the hematite surface was studied by DFT calculations using the Vienna Ab initio Simulation Package (VASP).[30,31] The {012} facet ("r-cut", equal to {$1\bar{1}02$}) was commonly observed in the naturally occurring and laboratory-synthesized hematite samples[32−34] and frequently exploited in geochemistry because it has a relatively low surface energy.[35,36] Moreover, high-resolution transmission electron microscopy (HRTEM) images revealed that {012} was the dominant surface in hematite samples. We therefore constructed a {012} hematite surface to perform DFT calculations. The {012} surface was completely protonated to simulate the real water/mineral interfacial environment. A $H_2AsO_4^-$ ion was used in the DFT calculations because $H_2AsO_4^-$ is the predominant As(V) species at pH 6.0.[37] The reaction adsorption energy (E_{ads}) of arsenate on the α-Fe_2O_3 {012} surface was calculated using the following equation: $E_{ads} = E_{arsenic/hematite} - E_{hematite} - E_{H_2AsO_4^-}$, where $E_{hematite}$ is the energy for the optimized {012} hematite slab plus one or two water molecules. $E_{H_2AsO_4^-}$ corresponded to the energy of a $H_2AsO_4^-$ ion. The details of the calculation parameters are presented in Text S4.

3. RESULTS AND DISCUSSION

3.1. Bulk Characterization. Hematite samples with different OVD concentrations were obtained through the treatment of defect-free hematite using $NaBH_4$ solutions with
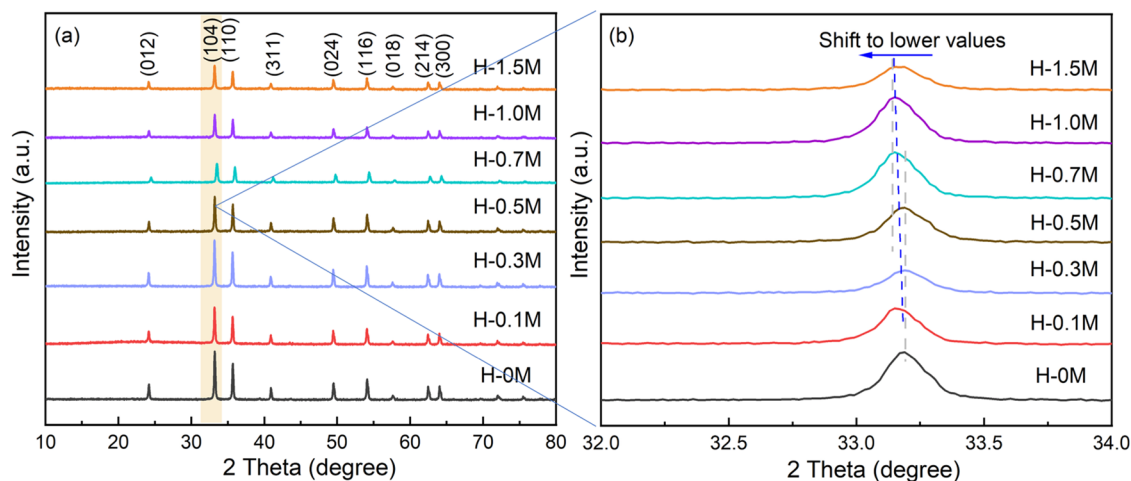
Figure 1. (a) XRD patterns of hematite samples treated by different concentrations of NaBH$_4$ and (b) their corresponding patterns at 32−34°.

different concentrations of 0.1, 0.3, 0.5, 0.7, 1.0, and 1.5 M, respectively (denoted as H-0.1M, H-0.3M, H-0.5M, H-0.7M, H-1.0M, and H-1.5M). The NaBH$_4$ reagent is an oxygen scavenger that has a strong reducibility, which is conducive to the formation of oxygen vacancies within a relatively short time.[27,38] The reaction between hematite and NaBH$_4$ for forming OVDs could be described as follows

$$\alpha - Fe_2O_3 + x/2\ BH_4^-$$
$$\rightarrow \alpha - Fe_2O_{3-x} + x/2BO_2^- + x\ H_2 \quad (1)$$
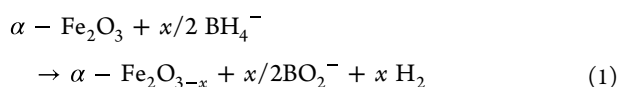
where x represents the stoichiometric number of oxygen vacancies in the structural formula of the hematite surface (α-Fe$_2$O$_3$). Figure S1 shows the color change of hematite powders from red to black when it is treated with NaBH$_4$. This phenomenon was also observed in other defect-containing minerals (e.g., TiO$_2$), i.e., the more defects in mineral are formed, the darker the mineral color appears.[39] This result suggests that the NaBH$_4$ treatment was feasible for generating OVDs in hematite. Figure 1a shows the XRD patterns of different hematite samples. The diffraction reflections of all as-synthesized samples were quite similar and were consistent with the XRD patterns of α-Fe$_2$O$_3$ reference in a crystallographic database (JCPDS 33−0664). No impurity reflections (e.g., zero-valent Fe, goethite, or maghemite) were observed in the patterns, suggesting that the NaBH$_4$ treatment did not alter the structure of hematite in this case. Remarkably, increasing NaBH$_4$ concentrations not only led to an obvious decrease in the crystallinity of the hematite samples but also resulted in a considerable shift of the reflection at ~33.2° (corresponding to the {104} facet) to lower degree values (Figure 1b). This phenomenon was also described before in the literature,[40] which was attributed to the lattice expansion due to the existence of oxygen vacancies. To confirm this observation, we calculated the cell volume of different hematite samples through Rietveld structure refinement of their corresponding XRD patterns (Figure S2a). As shown in Table S1, the fitted cell volume of hematite increased with increasing NaBH$_4$ concentrations, suggesting that lattice expansion occurred in hematite samples by the NaBH$_4$ treatment.

To illustrate whether the NaBH$_4$ treatment affected the morphology and exposed lattice facets, three typical hematite samples of H-0M, H-0.7M, and H-1.5M, which represent relatively low, medium, and high defect concentrations,

respectively, were analyzed by SEM and TEM. As shown in Figure S3, the three hematite samples exhibited a granular morphology, while the crystallinity of H-0.7M and H-1.5M samples was obviously lower than that of the H-0M sample. We observed that the edges of particles in the H-1.5M sample became irregular compared to those of the H-0M sample (Figure S3d,f). High-resolution TEM (HRTEM) images revealed that the lattice fringe of particles in the H-0M sample was 0.373 nm, which was assigned to the {012} facet (Figure S3g). After NaBH$_4$ treatment, H-0.7M and H-1.5M samples still showed the same exposed facet of {012}. The selected area electron diffraction (SAED) patterns revealed that the {110}, {113}, and {012} facets were also observed in the three hematite samples (Figure S3j,k,l), and no new rings corresponded to new phases of iron (oxyhydr)oxides and FeB compounds occurred. This result indicated that NaBH$_4$ treatment did not alter the hematite structure despite the presence of abundant oxygen vacancy defects, which was consistent with the XRD analysis. The TEM-EDS mapping showed that Fe and O are homogeneously distributed throughout the hematite sample (Figure S4). The proportion of oxygen decreased gradually from 68.49% to 56.54% with increasing NaBH$_4$ concentrations (Table S2). This result clearly demonstrated that the NaBH$_4$ treatment is suitable to produce oxygen vacancy defects, and the higher the NaBH$_4$ concentration, the more oxygen vacancy defects are present.

3.2. Defect Characteristics in Hematite. Positron annihilation lifetime (PAL) spectrometry has emerged as a unique and effective probe for identifying atomic defects with high sensitivity.[41−44] The positron lifetime can provide information about the type and size of defects.[45] Table 1 exhibits the fitting result of PAL spectra in H-0M, H-0.7M, and H-1.5M samples. As shown in Table 1, the PAL spectra of hematite samples can be decomposed into three distinct lifetime components, i.e., τ_1, τ_2, and τ_3.[46,47] The longest

Table 1. Positron Annihilation Lifetime Parameters of the Vacancies Bearing Hematite Samples

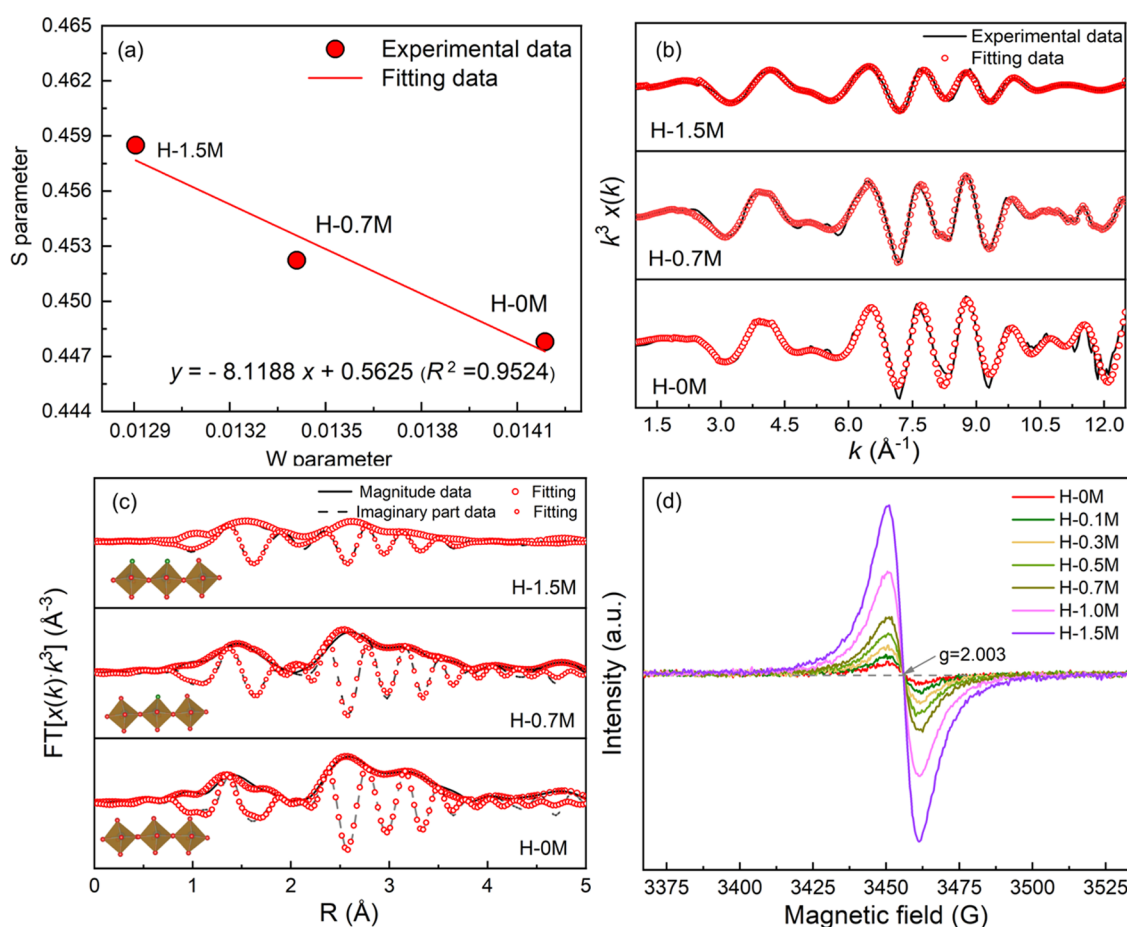| samples	τ_1 (ps)	I_1 (%)	τ_2 (ps)	I_2 (%)	τ_3 (ps)	I_3 (%)
H-0M	177.9	50.70	389.9	48.27	1747	1.03
H-0.7M	175.1	36.33	398.5	60.39	2146	3.28
H-1.5M	182.1	34.78	406.3	61.79	2152	3.43

Figure 2. (a) Variation of S and W parameters, Fourier-transformed (b) k space and (c) R space curves of EXAFS spectra (structure models of $[FeO_6]$ in the presence of oxygen vacancy, green is the oxygen atom to be removed), and (d) EPR spectra of different defective hematite samples.

lifetime component (τ_3, 1747−2152 ps) corresponded to the annihilation of ortho-positronium atoms formed in the large voids in materials.[48] The medium lifetime component (τ_2, 389.5−406.3 ps) was assigned to the positrons captured by large defects in the minerals, such as oxygen vacancy clusters.[49] The shortest component (τ_1) was generally attributed to the free annihilation of positrons in the defect-free bulk regions and tiny vacancies.[47,49−51] The relative intensity (I) gave the information on the distribution of these defects. For the H-0M sample, we found an extremely low concentration of defects due to the calcination treatment, as evidenced by TG-MS analysis discussed in the below section. However, its defects were still detected by PAL analysis, indicating that the PAL technique was a sensitive tool to probe the defects. In addition, it could be found that the I_2 in H-0.7M and H-1.5M samples was higher than those of I_1 and I_3 (Table 1), suggesting that a large abundance of large defects of oxygen vacancy clusters existed in the hematite samples after the $NaBH_4$ treatment.

The Doppler broadening of annihilation radiation (DBAR) records the momentum distribution of each electron that has been reported to be used to identify the defect type.[52] In this study, the evolution of vacancy defect types in three typical hematite samples of H-0M, H-0.7M, and H-1.5M was studied by DBAR. The S and W parameters derived from the Doppler spectra represent the relative contributions of low- and high-momentum electrons in the annihilation sites, respectively. According to the previous reports,[52,53] the information on defect type in the samples could be obtained from plotting the

W parameter as a function of the S parameter ($S−W$ plot). If there was only the same type of defect in the minerals, the $S−W$ plot could be fitted as a linear function.[53] Figure 2a exhibits the $S−W$ plots of three hematite samples (H-0M, H-0.7M, and H-1.5M). Interestingly, $S−W$ plots could be fitted well through a linear equation, as evidenced by its higher R^2 of 0.9524. This result combined with PAL analysis indicated that oxygen vacancy defects existed dominantly in the hematite samples, which were treated by $NaBH_4$.

To confirm the DBAR analysis, EXAFS was employed to investigate the atom coordination of Fe−Fe and Fe−O in the three hematite samples (H-0M, H-0.7M, and H-1.5M). Figure 2b shows the Fe K-edge EXAFS spectra of H-0M, H-0.7M, and H-1.5M samples. The three samples showed similar Fe K-edge EXAFS spectra, indicating that the $NaBH_4$ treatment did not alter the basic structure of the hematite samples. In addition, an obvious signal appeared at ~5.5 $Å^{-1}$ in the three samples, which was attributed to a typical crystalline iron oxide.[54] Figure 2c illustrates the Fourier-transformed (FT) EXAFS radial distribution functions of the three hematite samples. There were two shells of Fe−O and Fe−Fe that were observed in the FT EXAFS spectra. Artemis software was employed to obtain the coordination information through fitting their FT EXAFS spectra (Table S3). Two coordination structures appeared to exist in the Fe−O shell. The first one represents Fe−O_1 coordination with a bond length of 1.90−1.93 Å, and the second one could be assigned to the Fe−O_2 coordination with a bond length of 2.03−2.09 Å. The total Fe−O coordination
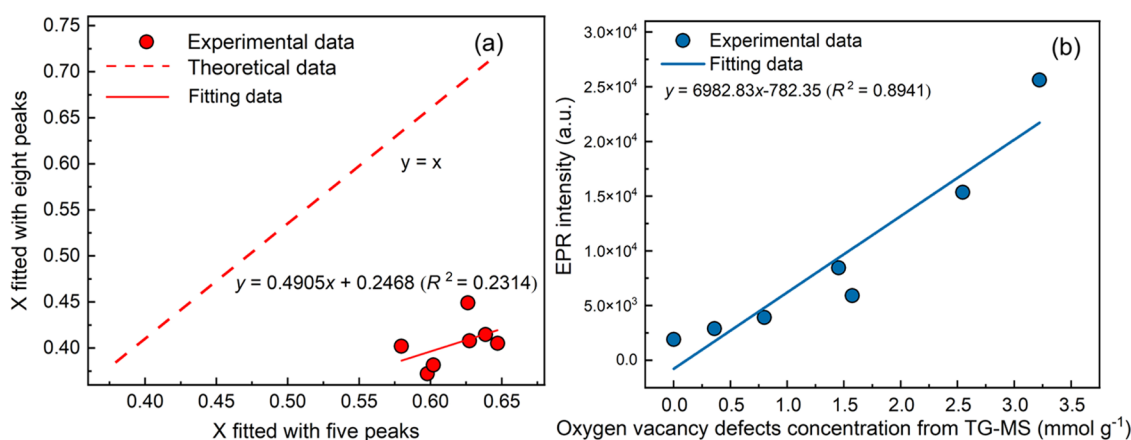
Figure 3. (a) Relationship of the OVD concentration obtained from Fe 2p XPS spectra through two fitting approaches reported in previous literature studies. (b) Relationship between TG-MS quantitative analysis results and EPR intensity results.

number (CN_{Fe-O}) of the H-0M sample was 6.2. Remarkably, the total CN_{Fe-O} values in the H-0.7M and H-1.5M samples decreased to 4.6 and 2.2, respectively. The relatively low CN_{Fe-O} values in the H-0.7M and H-1.5M samples indicated that there exist Fe or oxygen vacancies in the hematite structure. In addition, three coordination structures were observed in the Fe−Fe shell, corresponding to edge-sharing ($Fe-Fe_1$ and $Fe-Fe_2$) and corner-sharing ($Fe-Fe_3$) Fe−Fe coordination, respectively. The total Fe−Fe coordination number (CN_{Fe-Fe}) of the H-0M, H-0.7M, and H-1.5M samples was set as 8.0, which showed an excellent fitting result, evidenced by low R factor and low ΔE_0 values (Table S3). This result revealed that oxygen vacancies rather than Fe vacancies were the primary defect type in defective hematite samples. Moreover, we employed angle-resolved X-ray photoelectron spectroscopy (ARXPS) to collect the Fe 2p and O 1s spectra of three hematite samples (H-0.1M, H-0.7M, and H-1.5M) at surface depths of ∼3.5 and ∼10 nm, respectively (Figures S5 and S6). Interestingly, the ratios of Fe^{2+} to Fe^{3+} obtained from Fe 2p XPS spectra fitting for all hematite samples at a surface depth of ∼3.5 nm were obviously larger than those at a surface depth of ∼10 nm, indicating that Fe^{2+} species mainly distributed in the surface structure of hematite, rather than the subsurface structure. The relatively high Fe^{2+} fraction at a surface depth of ∼3.5 nm meant the occurrence of more oxygen vacancies in the surface structure.

3.3. Quantitation of Oxygen Vacancy Defect Concentration in Hematite. Although we had observed the OVDs in the hematite samples, quantifying the OVD concentration is still a challenge. Previous studies had employed EXAFS and XRD techniques to quantify the vacancies. However, the fitting process of the EXAFS spectrum is very complicated and involves several parameters, which may lead to a relatively high fitting error of ∼20%. Moreover, XRD analysis is not sensitive to a very low concentration of components (e.g., <5%). We therefore considered two possible approaches of XPS and TG-MS to make efforts for quantifying the OVD concentrations in our hematite samples. In general, the presence of oxygen vacancies may result in the change of the Fe oxidation state at the surface of hematite for maintaining charge balance[55,56]

$$—Fe^{3+}—O^{2-}—Fe^{3+}—O^{2-}—Fe^{3+}—$$
$$\rightarrow —Fe^{2+}—O^{2-}—Fe^{3+}—\square—Fe^{2+}— + \frac{1}{2}O_2 \qquad (2)$$
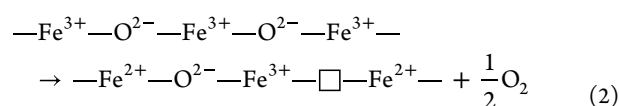
where the hollow block ($\square$) represents the oxygen vacancy in the hematite structure. The above reaction could be described as follows

$$\alpha − Fe_2O_3 \rightarrow Fe_y^{2+}Fe_{2-y}^{3+}O_{3-x}^{2-} + \frac{x}{2}O_2 \qquad (3)$$
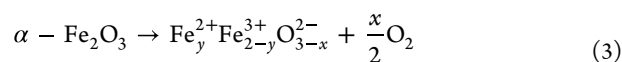
where y is the fraction of Fe^{2+} species in hematite. Therefore, the OVD concentration could be quantitatively calculated by measuring the Fe oxidation state through fitting their Fe 2p XPS spectra. In this study, we calculated the relative atomic ratio in the surface hematite of Fe^{2+} to Fe^{3+} using two methods for fitting Fe 2p XPS spectra (Figures S7 and S8, and Tables S4−S6), i.e., either a five-peak or eight-peak treatment.[57−59] Figure 3a shows the OVD concentration obtained from the eight-peak treatment as a function of that obtained from the five-peak treatment. Unfortunately, all of the points obviously gathered in a concentrated area, and the slope obtained through linear regression fitting was 0.4905 (R^2 = 0.2314), which was not close to the red dashed line. This result indicated that using the XPS technique for quantifying the OVD concentration was associated with a great uncertainty, which requires special attention. Moreover, we collected Fe K-edge XANES spectra of three typical hematite samples of H-0M, H-0.7M, and H-1.5M to further investigate the Fe oxidation state (Figure S9). The OVD concentrations of H-0M, H-0.7M, and H-1.5M samples obtained from the Fe K-edge XANES spectra fitting still exhibited a poor correlation with those obtained from the Fe2p XPS fitting (Figure S10).

Thermogravimetric (TG) analysis can be used to detect the change of hematite mass, and mass spectrometry (MS) can trace the evolution of gas signals (e.g., oxygen and water) during the reaction. Therefore, TG-MS may be a suitable approach to accurately quantify the OVD concentration in different samples. Figure S11 shows the TG-MS profiles of the seven hematite samples incubated in the presence of oxygen at temperatures ranging from 200 to 750 °C. For the H-0M sample, we observed no obvious increase or decrease of the weight in a 5% O_2/He atmosphere. Moreover, no O_2 and H_2O signals were observed in the MS profile of the H-0M sample, suggesting that the abundance of oxygen defects in the H-0M sample was too small to be detected by TG analysis. This was
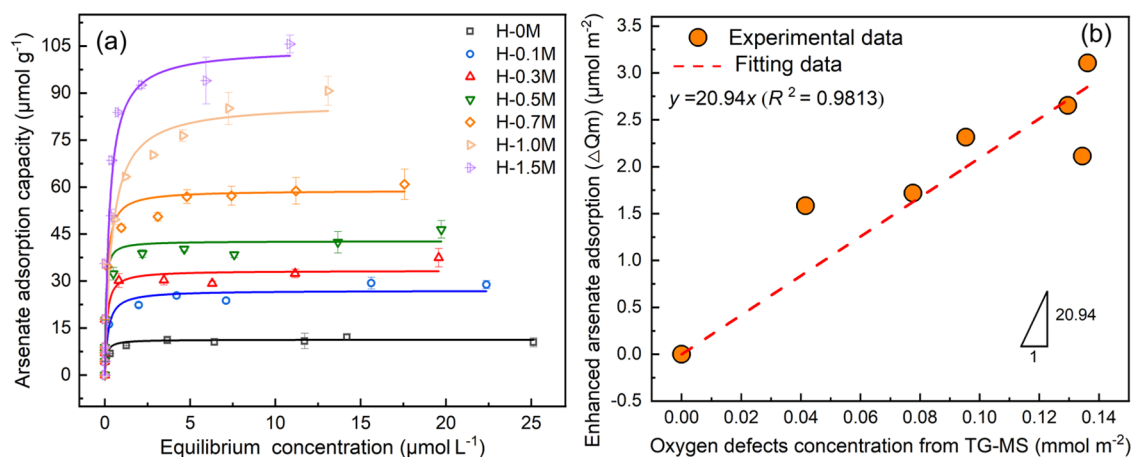
Figure 4. (a) Adsorption isotherm curves of different hematite samples with respect to As(V) at pH 6.0. Data was fitted using the Langmuir model. All of the experiments were performed three times. (b) Relationship between the oxygen vacancy concentration and arsenic adsorption capacity. The red line shows the linear fit with slope = 20.94 ± 1.69, R^2 = 0.9813.

attributed to the calcination treatment that sufficiently removed the defects in hematite. An obvious increase in weight of all NaBH$_4$-treated hematite samples was recorded by TG at temperatures of 300−600 °C. In addition, we observed O$_2$ signals in the MS profiles of hematite samples during the weight-increasing process, while H$_2$O MS signals did not appear. This indicated that the increased weight in all hematite samples can be attributed to O$_2$ consumption. i.e., oxygen molecules participated in the reaction to fill oxygen vacancies in hematite. The oxygen vacancy concentration of H-0.1M, H-0.3M, H-0.5M, H-0.7M, H-1.0M, and H-1.5M, calculated based on the weight change, was 0.36, 0.80, 1.58, 1.47, 2.56, and 3.24 mmol g^{-1}, respectively (Table S7). Electron paramagnetic resonance (EPR) analysis is very sensitive to the change of local environment that has been widely used to qualitatively characterize relative concentrations of oxygen vacancies in oxide minerals.[60−64] In this study, we employed EPR to further examine the results of the TG-MS analysis. Figure 2d illustrates the EPR spectra of different hematite samples. The EPR spectra of oxygen-deficient samples exhibited a strong signal of g = 2.003, owing to the electrons trapped in the defect sites.[65] This result confirmed the existence of a large number of oxygen vacancies arising from the reduction of hematite by NaBH$_4$, and the stronger the EPR signal, the higher the OVD concentrations were in the hematite samples. The evolution of the EPR signals as a function of OVD concentrations calculated from TG-MS analysis is shown in Figure 3b. Interestingly, it showed a good linear relationship between the OVD concentration and EPR signals, which could be described as a linear regression equation of $y = 982.83x − 782.35$ (R^2 = 0.8941), where x and y represent the OVD concentrations calculated from TG-MS analysis and from the EPR signals, respectively. We also employed another two unknown hematite samples (denoted as H-0.8M and H-1.3M, respectively) to confirm the reliability of the above formula for predicting the OVD concentration (Figure S12). To the best of our knowledge, this was the first time where a correlation between the quantitative method of TG-MS analysis and the qualitative approach of EPR was established for quantifying the oxygen vacancy defect concentration. As the cost and time consumption of TG-MS characterization was far higher than that of EPR analysis, the good linear relationship between TG-MS and EPR analysis

means that the low-cost EPR technique could be used to predict the OVD concentrations in hematite samples based on the above formula.

3.4. Contribution of Oxygen Vacancy Defects to Arsenate Immobilization on Hematite. To evaluate the effect of OVDs on arsenate adsorption by hematite samples, adsorption isotherm experiments for As(V) removal were carried out at pH 6.0. The Langmuir and Freundlich models were used in this study to fit their adsorption isotherm profiles (Figure S13). The maximum amounts of arsenate adsorbed by different hematite samples were calculated to compare their adsorption capacities (Table S8). As shown in Figure 4a, the Langmuir model could be used to well fit the adsorption isotherm curves of all defective hematite samples. For the H-0M sample, its maximum As(V) adsorption was 11.3 μmol g^{-1}. Interestingly, increasing the oxygen defect concentration led to an obvious increase in As(V) adsorption. When the OVD concentration of H-0.1M, H-0.3M, and H-0.5M samples increased to 0.36, 0.80, and 1.58 mmol g^{-1}, respectively, their corresponding maximum As(V) adsorption amount increased to 27.0, 33.3, and 42.8 μmol g^{-1}, respectively. The H-1.5M sample with the highest OVD concentration exhibited the highest As(V) adsorption (104.38 μmol g^{-1}). Moreover, XRD and Raman analyses revealed that the structure of the H-1.5M sample after treatment at 40 °C in an oven for 12 h had little change compared to that placed at room temperature (Figure S14), indicating that hematite with oxygen vacancies was very stable even after treatment at 40 °C. The successive fourth cycle runs for As(V) adsorption sample revealed that H-1.5M with the highest OVD concentration possessed excellent regeneration ability for arsenic removal (Figure S15). The adsorption free energy of hematite samples was calculated based on their isotherm adsorption measurements using the Langmuir model. Table S8 lists the adsorption free energy of different samples calculated from their corresponding Langmuir equilibrium constant (K_L, L/mmol) values. As shown in Figure S16, there was a correlation between the maximum adsorption amount (Q_{max}) and ΔG, indicating that vacancies in hematite increased the adsorption strength toward As(V). This result clearly demonstrated that OVDs played an important role in As(V) immobilization on hematite.

To quantify the contribution of OVDs to As(V) immobilization, the relationship between the oxygen vacancy
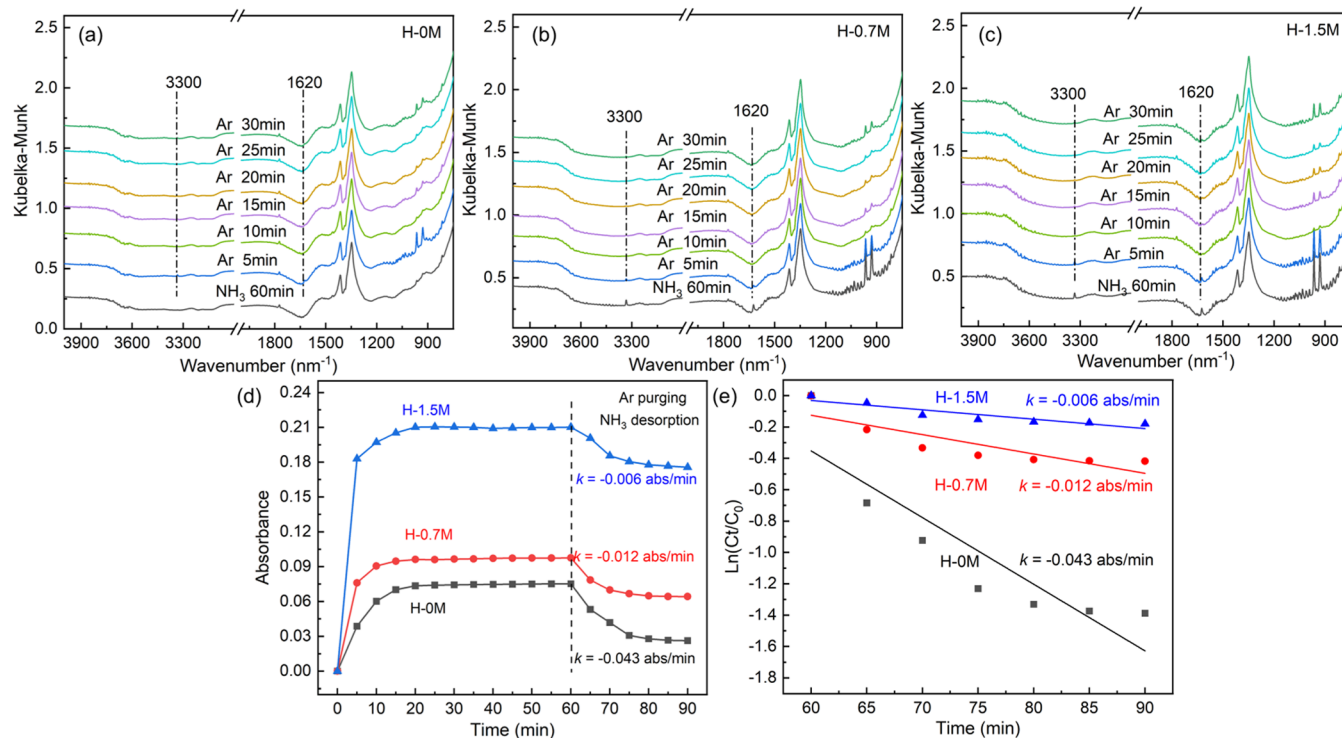
Figure 5. Evolution of DRIFT spectra for NH_3 adsorption/desorption on H-0M (a), H-0.7M (b), and H-1.5M (c) samples as a function of time. (d) Evolution of the peak intensity at ∼1620 cm^{-1} from the DRIFT spectra and (e) pseudo-first-order kinetics model for fitting NH_3 desorption on three hematite samples.

concentration calculated from TG-MS and the adsorption capacities of hematite samples was evaluated. Considering that different hematite samples have different specific surface areas (SSAs), the SSA-normalized adsorption capacity and OVD concentration were calculated to eliminate the surface area effect (Figure S13). Figure 4b illustrates the relationship between the enhanced adsorption amount (ΔQ_m, $\mu mol\ m^{-2}$) of hematite and the OVD concentration (mmol m^{-2}). We found that the adsorption amount of hematite linearly increased with increasing OVD concentration, which could be described by a linear regression equation of $\Delta Q_m = 20.94\ C_{def}$, as evidenced by its R^2 of 0.9813. This result means that increasing 1 mmol m^{-2} OVD concentration in hematite could improve the As(V) adsorption by 20.94 $\mu mol\ m^{-2}$ on hematite. In order to verify the reliability of the above linear equation, two additional samples of H-0.8M and H-1.3M were employed to evaluate their As(V) adsorption capacities under the same conditions (Table S9). The OVD concentration per unit surface areas of H-0.8M and H-1.3M samples were 0.11 and 0.13 mmol m^{-2}, respectively. The enhanced As(V) adsorption amounts (ΔQ_m) of the H-0.8M and H-1.3M samples calculated by the above equation were 2.36 and 2.65 μmol m^{-2}, respectively. Remarkably, the ΔQ_m values of the H-0.8M and H-1.3M samples obtained from adsorption isotherm fitting were 2.34 and 2.89 $\mu mol\ m^{-2}$, respectively, suggesting that the above equation could predict the contribution of OVDs to the arsenate immobilization.

3.5. Effect of Oxygen Vacancy Defects on Surface-Active Sites of Hematite. OVDs had been observed to promote the adsorption of arsenic on hematite, but the reasons why OVDs affected the adsorption of arsenic on hematite remained unclear. To illustrate whether the OVDs alter the distribution of active sites in hematite, in situ NH_3-DRIFT

spectra of three H-0M, H-0.7M, and H-1.5M hematite samples were collected (Figure 5). After NH_3 adsorption for 60 min, two obvious IR characteristic peaks at ∼1620 and ∼3300 cm^{-1} simultaneously appeared in the DRIFT spectra of three hematite samples. The intensity of two IR characteristic peaks in H-1.5M was higher than those in H-0.7M and H-0M samples, suggesting that NH_3 had strong adsorption on H-1.5M. The IR characteristic peaks at ∼1620 and ∼3300 cm^{-1} were attributed to the adsorbed NH_3 on Lewis acid sites.[66−70] Remarkably, no IR characteristic peaks at ∼1440 cm^{-1} and in the relatively high wavenumber region of 1850−1640 cm^{-1}, corresponding to Brønsted acid sites for NH_3 bound,[66−70] were observed in the DRIFT spectra of three samples. This result indicated that Lewis acid sites, rather than Brønsted acid sites, were the active sites for adsorption. Previous study defined the Lewis acid sites in hematite as undercoordinated Fe atoms on the surface.[71] The presence of OVDs on the hematite surface was therefore beneficial to generation of more undercoordinated Fe atoms, thereby forming more Lewis acid sites.

The bonding strength of surface complexes could be reflected by the strength of Lewis acid sites. To reveal the effect of OVD on the Lewis acid strength of hematite samples, the NH_3 desorption behavior on three hematite samples was recorded under subsequent Ar purging. As shown in Figure 5a−c, the intensity of IR characteristic peaks at ∼1620 cm^{-1} gradually decreased after Ar purging, indicating that NH_3 adsorbed at Lewis acid sites of hematite started to desorb. The pseudo-first-order kinetics model was used to fit the NH_3 desorption from the DRIFT spectra of three samples (Figure 5d,e). The obtained rate constant k for H-0M, H-0.7M, and H-1.5M samples was −0.043, −0.016, and −0.006 abs min^{-1}, respectively. The relatively large k in the H-1.5M sample meant that
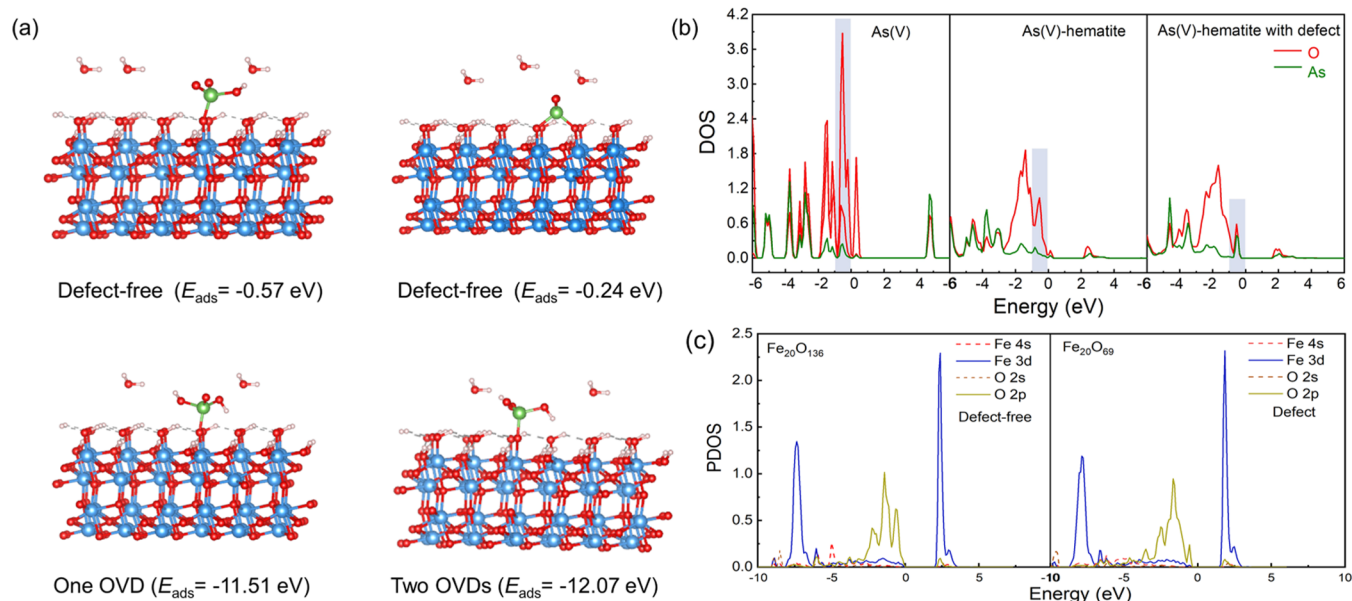
Figure 6. (a) Optimized structure of inner-sphere As(V) ($H_2AsO_4^-$) monodentate (upper left) and bidentate (upper right) complexes on the surface of the hematite slab with the absence and presence of one (lower left) and two (lower right) oxygen atom vacancies: white is for hydrogen atom, green is for arsenic atom, red is for oxygen atom, and blue is for Fe atom. (b) DOS plots of As(V) molecules before and after adsorption on perfect- and defect-hematite slabs. (c) PDOS plots of the Fe−O bonds after arsenic adsorption on hematite without and with one oxygen vacancy.

that it had a slow NH_3 desorption due to the strong bonding of NH_3 on Lewis acid sites compared to H-0M and H-0.7M samples.

3.6. Surface Complex of As(V) on Defective Hematite. ATR-FTIR was employed to illustrate the possible effect of OVDs on the surface complexes of As(V) on hematite. The FTIR spectra of H-0M, H-0.7M, and H-1.5M samples were recorded for the As−O characteristic peaks in the range of 950−700 cm^{-1}. As shown in Figure S17, the intensity of the IR peak in the range of 950−700 cm^{-1} gradually increased with reaction time, suggesting that As(V) adsorbed on three hematite samples. We selected FTIR spectra of three hematite samples after reaction for 6 h to analyze the surface complex structures (Figure S17d−f). For the H-0M sample, its FTIR spectrum could be decomposed into two strong peaks at ~836 and ~795 cm^{-1}. The H-0.7M and H-1.5M samples showed FTIR spectra similar to the H-0M sample, also with two resolved peaks at ~840 and ~790 cm^{-1} for H-0.7M and ~839 and ~789 cm^{-1} for H-1.5M, respectively. The IR peaks at ~790 and ~840 cm^{-1} were attributed to the As(V)−O−Fe stretching vibrations and the asymmetric As(V)−O vibrations in the monodentate singly protonated As(V) complex of = Fe−O−As(V)−O_2(OH), respectively.[71] This observation was also confirmed by the DFT calculation, i.e., the adsorption energy of arsenate on the pristine hematite slab in the form of the monodentate complex (−0.57 eV) was lower than that in the form of the bidentate complex (−0.24 eV) (Figure 6a), suggesting that the formation of the monodentate complex of = Fe−O−As(V)−O_2(OH) was more favorable than that of the bidentate complex of = (FeO)$_2$−As(V)−O_2.

The As K-edge EXAFS spectra of As-adsorbed hematite samples were collected to further reveal the effect of OVDs on the As−Fe complexes. Figure S18 exhibits Fourier-transformed k and R space curves of As K-edge EXAFS of H-0M, H-0.7M, and H-1.5M samples after the reaction with As(V). The fitting results of atomic distance (R_{As-O} and R_{As-Fe}), coordination number (N_{As-O} and N_{As-Fe}), and Debye−Waller factor (σ^2)

are shown in Table S10. The atomic distances at ~1.68 and ~3.47 Å for the arsenate-adsorbed H-0M sample corresponded to the first shell of As−O and the second shell of As−Fe, respectively. In the first As−O shell, the As atom was surrounded by four oxygen atoms with a N_{As-O} of 4.0, which was attributed to the molecular structure of an AsO_4 tetrahedron.[71] In the second As−Fe shell, the As atom was surrounded by one Fe atom with a CN of 1.0 and an R_{As-Fe} value of ~3.47 Å, suggesting the formation of a monodentate complex. Compared to the arsenate-adsorbed H-0M sample, the coordination number of N_{As-O} and N_{As-Fe} for arsenate-adsorbed H-0.7M and H-1.5M samples still maintained at 4.0 and 1.0, respectively, while their corresponding R_{As-Fe} values slightly changed to ~3.50 and ~3.41 Å. In addition, an As−O−O scattering path with a CN of 12 and an R value of 3.02−3.07 Å was observed in three samples, which also appeared in previous report.[71] This result indicated that oxygen vacancies did not alter the As−Fe complex model, which could be explained as follows. When the pristine hematite surface contained one oxygen vacancy, its surface structure had one undercoordinated Fe atom. In this case, one of the oxygen atoms in oxyanion As(V) readily inserted into the surface oxygen vacancy site and directly bonded with an under-coordinated Fe atom, thus forming a monodentate Fe−As complex model.

3.7. Bonding Analysis of As(V) on Defective Hematite. The influence of OVD on arsenic adsorption was further investigated by calculating the reaction adsorption energy of arsenic (E_{ads}) on the hematite slab in the presence and absence of oxygen vacancy using DFT calculation. Figure S19 exhibits a hematite surface with different oxygen vacancies. Based on the ATR-FTIR and As K-edge EXAFS analyses, a monodentate model of surface As−Fe complex was constructed for performing DFT calculations (Figure 6a). As shown in Figure 6a, the calculated E_{ads} on the perfect hematite was −0.57 eV. Interestingly, when the hematite slab contained one oxygen vacancy, the calculated E_{ads} significantly decreased to −11.51

eV. This phenomenon was also observed in previous work reported by Ou et al.,[31] who found that the energy of arsenate adsorbed on the oxygen-defective $Mg(OH)_2$ surface was ~10 times lower than that on the defect-free $Mg(OH)_2$ surface. Moreover, the calculated E_{ads} on the hematite slab with two oxygen vacancies further decreased to −12.07 eV compared to that on the hematite slab with one oxygen vacancy. This result indicated that the OVD concentration affected the arsenate adsorption energy. We constructed hematite slabs with different water contents to examine the effect of water molecules on the arsenate adsorption on hematite. The water molecules also affected the arsenate adsorption on hematite (Figure S20). However, the effect extent of water molecules was obviously lower than that of OVDs in the hematite structure. We examined the adsorption energy of one water molecule on the OVD site of defective hematite. The calculated E_{ads} of water on the OVD site was −8.23 eV (Figure S21), which was larger than that of the arsenate ion, suggesting that the arsenate species was more readily adsorbed on the OVD site than the water molecule.

To reveal the chemical bonding of arsenate on the defective hematite, the highest occupied molecular orbital (HOMO) and the lowest unoccupied molecular orbital (LUMO) of the arsenate species were analyzed before and after adsorption (Figure 6b). The DOS images revealed that the HOMO and LUMO of the single arsenate ion primarily consisted of oxygen atoms and an As atom, respectively. The electron density of HOMO gathered in a narrow area, suggesting an obvious localization of electron density in single arsenate species. Upon adsorption on pristine hematite, the energies of the HOMO and LUMO decreased, suggesting that delocalization of electron density occurred below the Fermi level (gray region). Compared to pristine hematite, a significant decrease in the energies of the HOMO and LUMO appeared after arsenate adsorption on defective hematite. This result indicated that OVDs promoted the delocalization of electron density, thereby enhancing arsenate bonding to form stable As−O−Fe complexes. The detailed chemical bonding was further illustrated by partial density of states (PDOS) of Fe−O atom pairs. Figure 6c exhibits the PDOS of As-bound O (2p, 2s) and Fe (3d, 4s) atoms after arsenic adsorption on the hematite slab without and with one oxygen vacancy. The overlap of PDOS below the Fermi level for Fe−O atom pairs was dominated by the contribution of electron sharing between the O (2p) and Fe (3d) orbitals for forming new Fe−O bonds. Remarkably, the intensity and shape of PDOS of the O (2s) orbital after arsenate adsorption on hematite with one vacancy became low and broad compared to that after arsenate adsorption on pristine hematite, suggesting that the delocalization of electron density between O (2p) and Fe (3d) orbitals in the former was higher than that in the latter. The relatively high delocalization of electron density between O (2p) and Fe (3d) after arsenate adsorption on defective hematite represents the strong binding between Fe and O atoms, which agreed well with DOS analysis and DFT calculations.

In this study, hematite samples with tunable oxygen vacancy defect concentrations were synthesized by treating defect-free hematite using $NaBH_4$ solutions ranging from 0 to 1.5 M. We employed several advanced characterization techniques to carefully examine the defect characteristics of hematite. A combination technique of TG-MS-EPR analysis was developed to quantitatively measure the oxygen vacancy defect concen-

tration in defective hematite. A good linear relationship between the OVD concentration and the enhanced adsorption amount caused by defects was established for the first time to better describe the degree of influence of vacancy defects on the arsenic immobilization. We combined both experimental and theoretical evidence to reveal the underlying mechanism of OVD effect on the surface-active sites, formation of the surface complex, and chemical bonding of arsenate on hematite. Fe-bearing minerals are the most active components in soil that strongly affect the immobilization of arsenic. Vacancy defects have been confirmed to exist widely in the soil environment and experimentally synthesized iron (oxyhydr)oxides due to various factors, such as temperature, impurities, and climatic and redox conditions.[72,73] The findings of this study not only help to rational design of highly efficient adsorbents by the strategy of tuning the vacancy defects in the structure of iron oxides but also provide new insights into the contribution of oxygen vacancy defects to the arsenate immobilization for precisely understanding the migration and fate of toxic arsenic in soils and sediments.

■ ASSOCIATED CONTENT

ⓢ Supporting Information

The Supporting Information is available free of charge at https://pubs.acs.org/doi/10.1021/acs.est.3c03441.

Details of sample preparation and sample characterization and other data (PDF)

■ AUTHOR INFORMATION

Corresponding Author

Jingtao Hou − *State Environmental Protection Key Laboratory of Soil Health and Green Remediation, Hubei Key Laboratory of Soil Environment and Pollution Remediation, College of Resources and Environment, Huazhong Agricultural University, Wuhan 430070, China;* ⓞ orcid.org/0000-0002-2472-8309; Email: houjt87@163.com

Authors

Juan Liu − *State Environmental Protection Key Laboratory of Soil Health and Green Remediation, Hubei Key Laboratory of Soil Environment and Pollution Remediation, College of Resources and Environment, Huazhong Agricultural University, Wuhan 430070, China*

Yongjin Xiang − *State Environmental Protection Key Laboratory of Soil Health and Green Remediation, Hubei Key Laboratory of Soil Environment and Pollution Remediation, College of Resources and Environment, Huazhong Agricultural University, Wuhan 430070, China*

Yiwen Chen − *State Key Laboratory of Particle Detection and Electronics, University of Science and Technology of China, Hefei 230026, China*

Hongjun Zhang − *State Key Laboratory of Particle Detection and Electronics, University of Science and Technology of China, Hefei 230026, China;* ⓞ orcid.org/0000-0002-4714-8809

Bangjiao Ye − *State Key Laboratory of Particle Detection and Electronics, University of Science and Technology of China, Hefei 230026, China*

Lu Ren − *School of Civil Engineering, Suzhou University of Science and Technology, Suzhou 215009, China;* ⓞ orcid.org/0000-0002-2166-1030

Wenfeng Tan − *State Environmental Protection Key Laboratory of Soil Health and Green Remediation, Hubei Key Laboratory of Soil Environment and Pollution Remediation, College of Resources and Environment, Huazhong Agricultural University, Wuhan 430070, China*

Andreas Kappler − *Geomicrobiology, Department of Geosciences, University of Tuebingen, Tuebingen 72076, Germany;* ⊙ orcid.org/0000-0002-3558-9500

Complete contact information is available at:
https://pubs.acs.org/10.1021/acs.est.3c03441

Notes
The authors declare no competing financial interest.

■ REFERENCES

(1) Chi, Z. L.; Yu, G. H.; Kappler, A.; Liu, C. Q.; Gadd, G. M. Fungal-Mineral Interactions Modulating Intrinsic Peroxidase-Like Activity of Iron Nanoparticles: Implications for the Biogeochemical Cycles of Nutrient Elements and Attenuation of Contaminants. *Environ. Sci. Technol.* **2022**, *56*, 672−680.

(2) Lafferty, B. J.; Loeppert, R. H. Methyl Arsenic Adsorption and Desorption Behavior on Iron Oxides. *Environ. Sci. Technol.* **2005**, *39*, 2120−2127.

(3) Manning, B. A.; Fendorf, S. E.; Goldberg, S. Surface Atructures and Stability of Arsenic on Goethite: Spectroscopic Evidence for Inner-Sphere Complexes. *Environ. Sci. Technol.* **1998**, *32*, 2383−2388.

(4) Xia, X.; Wang, J.; Hu, Y. F.; Liu, J.; Darma, A. I.; Jin, L.; Han, H.; He, C.; Yang, J. J. Molecular Insights into Roles of Dissolved Organic Matter in Cr(III) Immobilization by Coprecipitation with Fe(III) Probed by Stxm-Ptychography and Xanes Spectroscopy. *Environ. Sci. Technol.* **2022**, *56*, 2432−2442.

(5) Yan, L.; Chan, T. S.; Jing, C. Y. Mechanistic Study for Antimony Adsorption and Precipitation on Hematite Facets. *Environ. Sci. Technol.* **2022**, *56*, 3138−3146.

(6) Bidast, S.; Golchin, A.; Baybordi, A.; Zamani, A.; Naidu, R. The Effects of Non-Stabilised and Na-Carboxymethylcellulose-Stabilised Iron Oxide Nanoparticles on Remediation of Co-Contaminated Soils. *Chemosphere.* **2020**, *261*, No. 128123.

(7) Dong, K. W.; Xie, F.; Chang, Y. F.; Chen, C. L.; Wang, W.; Lu, D. K.; Gu, X. W. A Novel Strategy for the Efficient Decomposition of Toxic Sodium Cyanate by Hematite. *Chemosphere.* **2020**, *256*, No. 127047.

(8) Cárdenas-Hernández, P. A.; Anderson, K. A.; Murillo Gelvez, J.; Di Toro, D. M.; Allen, H. E.; Carbonaro, R. F.; Chiu, P. C. Reduction of 3-Nitro-1,2,4-Triazol-5-One (NTO) by the Hematite-Aqueous Fe(II) Redox Couple. *Environ. Sci. Technol.* **2020**, *54*, 12191−12201.

(9) Qu, C. C.; Chen, J. Z.; Mortimer, M.; Wu, Y. C.; Cai, P.; Huang, Q. Y. Humic Acids Restrict the Transformation and the Stabilization of Cd by Iron (Hydr)Oxides. *J. Hazard. Mater.* **2022**, *430*, No. 128365.

(10) Shen, Z.; Zhang, Z.; Li, T.; Yao, Q.; Zhang, T.; Chen, W. Facet-Dependent Adsorption and Fractionation of Natural Organic Matter on Crystalline Metal Oxide Nanoparticles. *Environ. Sci. Technol.* **2020**, *54*, 8622−8631.

(11) Zhang, J.; Coker, V. S.; Mosselmans, J. F. W.; Shaw, S. Adsorption of Octahedral Mono-Molybdate and Poly-Molybdate onto Hematite: A Multi-Technique Approach. *J. Hazard. Mater.* **2022**, *431*, No. 128564.

(12) Zong, M. R.; Song, D.; Zhang, X.; Huang, X. P.; Lu, X. C.; Rosso, K. M. Facet-Dependent Photodegradation of Methylene Blue by Hematite Nanoplates in Visible Light. *Environ. Sci. Technol.* **2021**, *55*, 677−688.

(13) Guo, T.; Jiang, L. S.; Huang, H. X.; Li, Y.; Wu, X. Y.; Zhang, G. K. Enhanced Degradation of Tetracycline in Water over Cu-Doped Hematite Nanoplates by Peroxymonosulfate Activation under Visible Light Irradiation. *J. Hazard. Mater.* **2021**, *416*, No. 125838.

(14) Liang, Y.; Jin, J. Z.; Xiang, Y. J.; Wang, M. X.; Xiong, J.; Hou, J. T.; Tan, W. F. Insights into the Improving Mechanism of Defect-Mediated As(V) Adsorption on Hematite Nanoplates. *Chemosphere.* **2021**, *280*, No. 130597.

(15) Qian, B. B.; Liu, C.; Lu, J.; Jian, M. P.; Hu, X. Y.; Zhou, S.; Hosseini, T.; Etschmann, B.; Zhang, X. W.; Wang, H. T.; Zhang, L. Synthesis of in-Situ Al^{3+}-Defected Iron Oxide Nanoflakes from Coal Ash: A Detailed Study on the Structure, Evolution Mechanism and Application to Water Remediation. *J. Hazard. Mater.* **2020**, *395*, No. 122696.

(16) Jeong, G. J.; Kim, J.; Park, M.; Seo, M.; Hwang, S. M.; Kim, Y.; Kim, Y.; Kim, J. H.; Dou, S. X. Core−Shell Structured Silicon Nanoparticles@TiO_{2-x}/Carbon Mesoporous Microfiber Composite as a Safe and High-Performance Lithium-Ion Battery Anode. *ACS Nano.* **2014**, *8*, 2977−2985.

(17) Ackermann, R. J.; Garg, S. P.; Rauh, E. G. The Lower Phase Boundary of ZrO_{2-x}. *J. Am. Ceram. Soc.* **1978**, *61*, 275−276.

(18) Bellakhal, N.; Draou, K.; Brisset, J. L. Electrochemical Investigation of Copper Oxide Films Formed by Oxygen Plasma Treatment. *J. Appl. Electrochem.* **1997**, *27*, 414−421.

(19) McCammon, C. A. Magnetic Properties of Fe_xO ($x > 0.95$): Variation of Néel Temperature. *J. Magn. Magn. Mater.* **1992**, *104−107*, 1937−1938.

(20) Hong, Z. B.; Fang, L. P.; Zhong, S. X.; Liu, K.; Li, F. B. Fe(II)-Mediated Activation of Oxygen by Goethite for the As(III) Oxidation and the Mechanisms. *Chin. Sci. Bull.* **2020**, *65*, 997−1008.

(21) Notini, L.; Byrne, J. M.; Tomaszewski, E. J.; Latta, D. E.; Zhou, Z.; Scherer, M. M.; Kappler, A. Mineral Defects Enhance Bioavailability of Goethite toward Microbial Fe(III) Reduction. *Environ. Sci. Technol.* **2019**, *53*, 8883−8891.

(22) Notini, L.; Latta, D. E.; Neumann, A.; Pearce, C. I.; Sassi, M.; N'Diaye, A. T.; Rosso, K. M.; Scherer, M. M. The Role of Defects in Fe(II)−Goethite Electron Transfer. *Environ. Sci. Technol.* **2018**, *52*, 2751−2759.

(23) Mladin, G.; Mihaela, C.; Adina, N.; Narcis, D.; Petru, N.; Paula, I.; Cătălin, I. Silica- Iron Oxide Nanocomposite Enhanced with Porogen Agent Used for Arsenic Removal. *Materials.* **2022**, *15*, No. 5366.

(24) Yin, J.; Yang, J.; Li, Y.; Xiang, Z.; Yang, T.; Wang, J.; Xu, T.; Wang, Q.; Wang, W. Photocatalytic Oxidation Activity Enhanced by Iron-Oxalate Chelates for Fenton-Like Oxidation of As(III) in Oxalate Systems. *J. Environ. Chem. Eng.* **2022**, *10*, No. 108232.

(25) Ji, M. F.; Arwa, A. A.; Majdi, A.; Liu, H.; Ali, I.; Marzouki, R. Remediation of Mine Polluted Soil with Nano-Enhanced Materials: Development of Extreme Learning Machine Approaches. *Chemosphere.* **2022**, *307*, No. 135772.

(26) Lund, T. J.; Koretsky, C. M.; Landry, C. J.; Schaller, M. S.; Das, S. Surface Complexation Modeling of Cu(II) Adsorption on Mixtures of Hydrous Ferric Oxide and Kaolinite. *Geochem. Trans.* **2008**, *9*, No. 9.

(27) Sun, S.; Zhai, T.; Liang, C.; Savilov, S. V.; Xia, H. Boosted Crystalline/Amorphous Fe_2O_{3-x} Core/Shell Heterostructure for Flexible Solid-State Pseudocapacitors in Large Scale. *Nano Energy.* **2018**, *45*, 390−397.

(28) Huang, Y. C.; Li, K. S.; Li, S. Q.; Lin, Y.; Liu, H.; Tong, Y. X. Ultrathin Bi_2MoO_6 Nanosheets for Photocatalysis: Performance Enhancement by Atomic Interfacial Engineering. *ChemistrySelect.* **2018**, *3*, 7423−7428.

(29) Hong, J.; Liu, L. H.; Luo, Y.; Tan, W. F.; Qiu, G. H.; Liu, F. Photochemical Oxidation and Dissolution of Arsenopyrite in Acidic Solutions. *Geochim. Cosmochim. Acta* **2018**, *239*, 173−185.

(30) Kresse, G.; Furthmüller, J. Efficient Iterative Schemes for Ab Initio Total-Energy Calculations Using a Plane-Wave Basis Set. *Phys. Rev. B.* **1996**, *54*, 11169−11186.

(31) Ou, X.; Liu, X.; Liu, W.; Rong, W.; Li, J.; Lin, Z. Surface Defects Enhance the Adsorption Affinity and Selectivity of $Mg(OH)_2$ Towards As(V) and Cr(VI) Oxyanions: A Combined Theoretical and Experimental Study. *Environ. Sci.: Nano.* **2018**, *5*, 2570−2578.

(32) McBriarty, M. E.; Stubbs, J. E.; Eng, P. J.; Rosso, K. M. Potential-Specific Structure at the Hematite−Electrolyte Interface. *Adv. Funct. Mater.* **2018**, *28*, No. 1705618.

(33) McBriarty, M. E.; von Rudorff, G. F.; Stubbs, J. E.; Eng, P. J.; Blumberger, J.; Rosso, K. M. Dynamic Stabilization of Metal Oxide−Water Interfaces. *J. Am. Chem. Soc.* **2017**, *139*, 2581−2584.

(34) Zhu, G.; Sushko, M. L.; Loring, J. S.; Legg, B. A.; Song, M.; Soltis, J. A.; Huang, X. P.; Rosso, K. M.; De Yoreo, J. J. Self-Similar Mesocrystals Form Via Interface-Driven Nucleation and Assembly. *Nature.* **2021**, *590*, 416−422.

(35) Huang, X. P.; Hou, X. J.; Zhang, X.; Rosso, K. M.; Zhang, L. Z. Facet-Dependent Contaminant Removal Properties of Hematite Nanocrystals and Their Environmental Implications. *Environ. Sci. Nano.* **2018**, *5*, 1790−1806.

(36) Mackrodt, W. C.; Davey, R. J.; Black, S. N.; Docherty, R. The Morphology of α-Al_2O_3 and α-Fe_2O_3: The Importance of Surface Relaxation. *J. Cryst. Growth.* **1987**, *80*, 441−446.

(37) Smedley, P. L.; Kinniburgh, D. G. A Review of the Source, Behaviour and Distribution of Arsenic in Natural Waters. *Appl. Geochem.* **2002**, *17*, 517−568.

(38) Tan, H.; Zhao, Z.; Zhu, W.-b.; Coker, E. N.; Li, B.; Zheng, M.; Yu, W.; Fan, H.; Sun, Z. Oxygen Vacancy Enhanced Photocatalytic Activity of Pervoskite $SrTiO_3$. *ACS Appl. Mater. Interfaces* **2014**, *6*, 19184−19190.

(39) Ou, G.; Xu, Y. S.; Wen, B.; Lin, R.; Ge, B. H.; Tang, Y.; Liang, Y. W.; Yang, C.; Huang, K.; Zu, D.; Yu, R.; Chen, W. X.; Li, J.; Wu, H.; Liu, L. M.; Li, Y. D. Tuning Defects in Oxides at Room temperature by Lithium Reduction. *Nat. Commun.* **2018**, *9*, No. 1302.

(40) Chen, H. J.; Lim, C.; Zhou, M. Z.; He, Z. Y.; Sun, X.; Li, X. B.; Ye, Y. J.; Tan, T.; Zhang, H.; Yang, C. H.; Han, J. W.; Chen, Y. Activating Lattice Oxygen in Perovskite Oxide by B-Site Cation Doping for Modulated Stability and Activity at Elevated Temperatures. *Adv. Sci.* **2021**, *8*, No. 2102713.

(41) Ling, L. L.; Jiao, L.; Liu, X. S.; Dong, Y.; Yang, W.; Zhang, H. J.; Ye, B. J.; Chen, J.; Jiang, H. L. Potassium-Assisted Fabrication of Intrinsic Defects in Porous Carbons for Electrocatalytic CO_2 Reduction. *Adv. Mater.* **2022**, *34*, No. 2205933.

(42) Tang, Z.; Hasegawa, M.; Shimamura, T.; Nagai, Y.; Chiba, T.; Kawazoe, Y.; Takenaka, M.; Kuramoto, E.; Iwata, T. Stable Vacancy Clusters in Neutron-Irradiated Graphite: Evidence for Aggregations with a Magic Number. *Phys. Rev. Lett.* **1999**, *82*, 2532−2535.

(43) Wang, C.; Cai, Z. L.; Xie, W.; Jiao, Y.; Liu, L.; Gong, L.; Zhang, Q. W.; Ma, X. H.; Zhang, H. J.; Luo, S. J. Finely Tuning the Microporosity in Dual Thermally Crosslinked Polyimide Membranes for Plasticization Resistance Gas Separations. *J. Membr. Sci.* **2022**, *659*, No. 120769.

(44) Zhang, H. J.; Sellaiyan, S.; Kakizaki, T.; Uedono, A.; Taniguchi, Y.; Hayashi, K. Effect of Free-Volume Holes on Dynamic Mechanical Properties of Epoxy Resins for Carbon-Fiber-Reinforced Polymers. *Macromolecules.* **2017**, *50*, 3933−3942.

(45) Zhu, H. P.; Wang, Z. G.; Gao, X.; Cui, M. H.; Li, B. S.; Sun, J. R.; Yao, C. F.; Wei, K. F.; Shen, T. L.; Pang, L. L.; Zhu, Y. B.; Li, Y. F.; Wang, J.; Song, P.; Zhang, P.; Cao, X. Z. Positron Annihilation Doppler Broadening Spectroscopy Study on Fe-Ion Irradiated NHs Steel. *Nucl. Instrum. Methods Phys. Res., Sect. B* **2015**, *344*, 5−10.

(46) Guan, M. L.; Xiao, C.; Zhang, J.; Fan, S. J.; An, R.; Cheng, Q. M.; Xie, J. F.; Zhou, M.; Ye, B. J.; Xie, Y. Vacancy Associates Promoting Solar-Driven Photocatalytic Activity of Ultrathin Bismuth Oxychloride Nanosheets. *J. Am. Chem. Soc.* **2013**, *135*, 10411−10417.

(47) Liu, X. W.; Zhou, K. B.; Wang, L.; Wang, B. Y.; Li, Y. D. Oxygen Vacancy Clusters Promoting Reducibility and Activity of Ceria Nanorods. *J. Am. Chem. Soc.* **2009**, *131*, 3140−3141.

(48) Chang, S. J.; Li, M.; Hua, Q.; Zhang, L. J.; Ma, Y. S.; Ye, B. J.; Huang, W. X. Shape-Dependent Interplay between Oxygen Vacancies and Ag−CeO_2 Interaction in Ag/CeO_2 Catalysts and Their Influence on the Catalytic Activity. *J. Catal.* **2012**, *293*, 195−204.

(49) Kong, M.; Li, Y. Z.; Chen, X.; Tian, T. T.; Fang, P. F.; Zheng, F.; Zhao, X. J. Tuning the Relative Concentration Ratio of Bulk Defects to Surface Defects in TiO_2 Nanocrystals Leads to High Photocatalytic Efficiency. *J. Am. Chem. Soc.* **2011**, *133*, 16414−16417.

(50) Shi, W. Q.; Li, Y. Z.; Hou, J. T.; Lv, H. Q.; Zhao, X. J.; Fang, P. F.; Zheng, F.; Wang, S. J. Densely Populated Mesopores in Microcuboid CeO_2 Crystal Leading to a Significant Enhancement of Catalytic Activity. *J. Mater. Chem. A* **2013**, *1*, 728−734.

(51) Wang, L.; Fei, W. Y.; Yan, Z.; Bo, Y. Y.; Hong, H.; Bo, Q. X.; Yi, W. B. Shape Dependence of Nanoceria on Complete Catalytic Oxidation of O-Xylene. *Catal. Sci. Technol.* **2016**, *6*, 4840−4848.

(52) Kumar, K. V. A.; Ningaraju, S.; Munirathnamma, L. M.; Ravikumar, H. B.; Ranganathaiah, C. Electron Beam Induced Microstructural Changes and Electrical Conductivity in Bakelite Polymer Rpc Detector Material: A Positron Lifetime Study. *J. Phys.: Conf. Ser.* **2015**, *618*, No. 012032.

(53) Szpala, S.; Asoka-Kumar, P.; Nielsen, B.; Peng, J. P.; Hayakawa, S.; Lynn, K. G.; Gossmann, H. J. Defect Identification Using the Core-Electron Contribution in Doppler-Broadening Spectroscopy of Positron-Annihilation Radiation. *Phys. Rev. B* **1996**, *54*, 4722−4731.

(54) Ona-Nguema, G.; Morin, G.; Juillot, F.; Calas, G.; Brown, G. E. EXAFS Analysis of Arsenite Adsorption onto Two-Line Ferrihydrite, Hematite, Goethite, and Lepidocrocite. *Environ. Sci. Technol.* **2005**, *39*, 9147−9155.

(55) Hou, J. T.; Ni, C. L.; Ren, L.; Yin, H.; Wang, M. X.; Tan, W. F. Simultaneous Introduction of K^+ and Rb^+ into OMS-2 Tunnels as an Available Strategy for Substantially Increasing the Catalytic Activity for Benzene Elimination. *Environ. Res.* **2020**, *191*, No. 110146.

(56) Ni, C. L.; Hou, J. T.; Wang, Z. W.; Li, Y. Z.; Ren, L.; Wang, M. X.; Yin, H.; Tan, W. F. Enhanced Catalytic Activity of OMS-2 for Carcinogenic Benzene Elimination by Tuning Sr^{2+} Contents in the Tunnels. *J. Hazard. Mater.* **2020**, *398*, No. 122958.

(57) Bhargava, G.; Gouzman, I.; Chun, C. M.; Ramanarayanan, T. A.; Bernasek, S. L. Characterization of the "Native" Surface Thin Film on Pure Polycrystalline Iron: A High Resolution XPS and TEM Study. *Appl. Surf. Sci.* **2007**, *253*, 4322−4329.

(58) Lin, T. C.; Seshadri, G.; Kelber, J. A. A Consistent Method for Quantitative XPS Peak Analysis of Thin Oxide Films on Clean Polycrystalline Iron Surfaces. *Appl. Surf. Sci.* **1997**, *119*, 83−92.

(59) Mahajan, J.; Jeevanandam, P. Synthesis of $TiO_2@\alpha$-Fe_2O_3 Core−Shell Heteronanostructures by Thermal Decomposition Approach and Their Application Towards Sunlight-Driven Photodegradation of Rhodamine B. *New. J. Chem.* **2018**, *42*, 2616−2626.

(60) Han, G. W.; Xu, F. Y.; Cheng, B.; Li, Y. J.; Yu, J. G.; Zhang, L. Y. Enhanced Photocatalytic H_2O_2 Production over Inverse Opal ZnO@ Polydopamine S-Scheme Heterojunctions. *Appl. Surf. Sci.* **2022**, *38*, No. 2112037.

(61) Juguilon, C.; Wang, Z. Y.; Wang, Y.; Enrick, M.; Jamaiyar, A.; Xu, Y. Y.; Gadd, J.; Chen, W. L.; Pu, A.; Kolz, C.; Ohanyan, V.; Chen, Y. R.; Hardwick, J.; Zhang, Y. Q.; Chilian, W. M.; Yin, L. Y. Mechanism of the Switch from NO to H_2O_2 in Endothelium-Dependent Vasodilation in Diabetes. *Basic Res. Cardiol.* **2022**, *117*, No. 2.

(62) Karlsson, E. B. Internal Dynamics in Condensed Matter, as Studied by Spin Relaxation: Some Examples from 75 Years. *Eur. Phys. J. H.* **2022**, *47*, No. 4.

(63) Ren, L.; Zhong, Y. H.; Xu, J. Y.; Chen, J. X.; Zou, T.; Liao, X. L.; Chen, Z. F.; Yu, L. Nano $Fe_{3-X}Cu_xO_4$ as the Heterogeneous

Catalyst in an Advanced Oxidation Process for Excellent Peroxymonosulfate Activation toward Climbazole Degradation. *Chem. Eng. J.* **2022**, *439*, No. 135553.

(64) Wang, Z. W.; Liu, Z.; Huang, J. Y.; Chen, Y.; Su, R. D.; He, J. K.; Lv, G. C.; Gao, B. Y.; Zhou, W. Z.; Wang, Y.; Wang, Z. N.; Li, Q. Zr$_6$O$_8$-Porphyrinic MOFs as Promising Catalysts for the Boosting Photocatalytic Degradation of Contaminants in High Salinity Wastewater. *Chem. Eng. J.* **2022**, *440*, No. 135883.

(65) Buryi, M.; Babin, V.; Artemenko, A.; Remes, Z.; Decka, K.; Micova, J. Hydrothermally Grown ZnO:Mo Nanorods Exposed to X-Ray: Luminescence and Charge Trapping Phenomena. *Appl. Surf. Sci.* **2022**, *585*, No. 152682.

(66) Ma, L.; Cheng, Y. S.; Cavataio, G.; McCabe, R. W.; Fu, L. X.; Li, J. H. In Situ Drifts and Temperature-Programmed Technology Study on Nh$_3$-SCR of Nox over Cu-SSZ-13 and Cu-SAPO-34 Catalysts. *Appl. Catal., B* **2014**, *156−157*, 428−437.

(67) Sjövall, H.; Fridell, E.; Blint, R. J.; Olsson, L. Identification of Adsorbed Species on Cu-ZSM-5 under NH$_3$ SCR Conditions. *Top. Catal.* **2007**, *42*, 113−117.

(68) Wang, D.; Zhang, L.; Kamasamudram, K.; Epling, W. S. In Situ-Drifts Study of Selective Catalytic Reduction of NOx by NH$_3$ over Cu-Exchanged SAPO-34. *ACS Catal.* **2013**, *3*, 871−881.

(69) Zecchina, A.; Marchese, L.; Bordiga, S.; Pazè, C.; Gianotti, E. Vibrational Spectroscopy of NH$_4^+$ Ions in Zeolitic Materials: An Ir Study. *J. Phys. Chem. B.* **1997**, *101*, 10128−10135.

(70) Zhu, H. Y.; Kwak, J. H.; Peden, C. H. F.; Szanyi, J. In Situ Drifts-MS Studies on the Oxidation of Adsorbed NH$_3$ by NOx over a Cu-SSZ-13 Zeolite. *Catal. Today.* **2013**, *205*, 16−23.

(71) Yan, L.; Chan, T. S.; Jing, C. Y. Arsenic Adsorption on Hematite Facets: Spectroscopy and DFT Study. *Environ. Sci. Nano.* **2020**, *7*, 3927−3939.

(72) Zheng, Q.; Tu, S. X.; Chen, Y. W.; Zhang, H. J.; Hartley, W.; Ye, B. J.; Ren, L.; Xiong, J.; Tan, W. F.; Kappler, A.; Hou, J. T. Micropore Sites in Ferrihydrite Are Responsible for Its Higher Affinity Towards As(III) Relative to As(V). *Geochim. Cosmochim. Acta.* **2023**, *348*, 27−40.

(73) Hou, J. T.; Tan, X. K.; Xiang, Y. J.; Zheng, Q.; Chen, C.; Sha, Z. J.; Ren, L.; Wang, M. X.; Tan, W. F. Insights into the Underlying Effect of Fe Vacancy Defects on the Adsorption Affinity of Goethite for Arsenic Immobilization. *Environ. Pollut.* **2022**, *314*, No. 120268.